Research paper

Numerical study on modeling the soil footpad interaction of lunar soft landers at touchdown

T. Pucker

HafenCity University, Henning-Voscherau-Platz 1, Hamburg, 22605, Germany

ARTICLE INFO

ABSTRACT

Soft landers are a common systems for planetary exploration and have been successfully landed on Moon, Mars and the comet Churyumov–Gerasimenko. In this study numerical simulations of the touchdown process of soft landers on the moon surface are presented. The focus is on the soil footpad interaction and the resulting loading on the primary strut of the landing gear. Main influence parameters like slope inclination, touchdown velocities and soil properties are varied to show each individual influence on the structural loading of the landing gear. The numerical simulations are done using the CEL-Method allowing for significant soil deformation at touchdown.

1. Introduction

The soft landing of robotic spacecraft on lunar terrain has become an integral part of lunar exploration. Recently, the Indian mission Chandrayaan-3 successfully landed a soft lander on the lunar surface (Fig. 1). In contrast, the Russian spacecraft Luna 25 was destroyed upon landing a few days before, indication the need for better understanding of the risks associated with the landing procedure. Focusing on the geotechnical topics, the risks associated with the landing procedure are unexpected ground conditions such as boulders on or below the surface, craters and slopes. These conditions can result in structural damage due to unexpected loadings, unstable footings after touchdown or turning over of the structure.

The interaction between the footpad and the soil is of particular interest, because it defines the structural load on the landing gear at touchdown. In addition the footpad acts as a shallow foundation to ensure the stability of the structure after touchdown. The mobilized reaction forces in the vertical and horizontal directions and the penetration of the footpad are crucial in the design of landing gears for soft landers. To prevent severe damage to the landing gear, energy absorbers such as honeycomb cartridges are integrated into the landing gear. Such a system can prevent damage from high impact loads. Penetration of the footpad improves the horizontal bearing capacity, because the soil strength typically increases with increasing depth. On the other hand, a minimum clearance between the bottom of the lander and the lunar surface needs to be ensured to prevent damage to the lander and, if needed, to allow an engine to ascend the lander for a return mission (e.g. the Apollo missions).

This study investigates the soil footpad interaction at the touchdown of a soft lander. While the study focuses on the moon environment,

soft landers are also used to explore other planets and objects such as comets. Famous examples are the viking missions that successfully landed on Mars and the Phliae lander that successfully landed on the surface of the comet Churyumov–Gerasimenko.

The interaction between the footpad and lunar soil surface has been investigated intensively by NASA (1968) for the preparation of the Apollo lunar landings between 1969 and 1972. For the viking missions a detailed assessment of the landing performance including several Monte-Carlo analyses was performed as described by Muraca et al. (1975). More recent investigations including full-scale tests of touchdown situations are documented by Witte et al. (2010) and Witte (2015).

Zheng et al. (2018) analyze the touchdown of a soft lander using the Finite Element Method (FEM) with explicit time integration scheme. The software packages Abaqus and LS-Dyna are compared to ensure simulation accuracy and reliability. Although the components of the soft lander are modeled in detail, the lunar surface is modeled as a rigid plane surface. This approach implies a significant simplification of the soil reactions. The dynamic response of lunar regolith during landing impact is studied by Che et al. (2018). Model scale tests and FEM simulations are performed using the software package Abaqus Explicit. The soil is modeled as a linear elastic, ideal plastic material. The study focuses on the wave propagation in the soil.

A detailed focus on the soil reaction at touchdown is presented in Yuncheng et al. (2020). The authors performed a numerical study of the soil footpad interaction using the Discrete Element Method (DEM). The size and properties of the DEM particles are chosen to represent the properties of the grains of lunar regolith. Because of the extremely

high number of soil particles affected by the touchdown underneath one footpad, the study has been performed in 2D using a small section of soil.

Ji and Liang (2021) model the touchdown process of a softlander by combining different numerical approaches. The lander is modeled with FEM using shell and beam elements. The motion characteristics of the lander are calculated using multibody dynamics (MBD) and the soil is modeled using DEM. Since the soil volume that needs to be considered involves a large number of soil grains, the DEM particles are increased in size up to 45 cm. Therefore, the DEM domain allows for large deformations; however the particles do not represent the actual soil grain behavior.

Another numerical study using the Abaqus Explicit software package is presented by Liang et al. (2022). The study models the soil in a FEM domain with a linear elastic, ideal plastic material. This approach does not allow for large soil deformations underneath the footpad without risking mesh distortion problems. Additionally, only a quarter of the soft lander, including one leg, is modeled in the study. Therefore, the influence of an inclined soil surface is not investigated. Wang et al. (2023) present a 6-DOF theoretical dynamic model to simulate the touch down of a soft lander. This dynamic model is compared to a multi-body model calculated using MSC Adams. Consequently, the importance of accurately modeling the friction interaction between the footpad and soil is highlighted.

Yin et al. (2023) investigate the impact of a lander footpad on the asteroid regolith and develop a macro model to calculate the normal force on the footpad. The macro model is calibrated using a parametric study based on the Discrete Element Method (DEM). The DEM allows the modeling of large deformations and dynamic impacts. However, the DEM particles used in this study do not reflect the actual size and shape of the asteroid regolith and can only be seen as a strongly simplified soil model.

A numerical simulation of the touchdown process focusing on the soil footpad interaction and the resulting forces in the landing gear of the spacecraft was used in this study to investigate the influence of touchdown velocity, soil properties and surface slope. The presented approach allows for a detailed investigation of the footpad soil interaction because the soil is modeled as a continuum. The Coupled Eulerian–Lagrangian-Method (CEL) applied in this study allows for dynamic loading and large soil deformation, which is expected to occur when the footpads penetrate the lunar regolith. The quality of the soil response depends on the applied constitutive model and can be enhanced depending on the effects that shall be investigated. Because the stiffness of the landing gear and the stiffness of the soil are modeled accurately, its interaction can be calculated more realistically than in previous studies where either the soil or the landing gear was considered to be rigid.

2. Soft lander model

A soft lander with four legs was investigated. The soft lander modeled in this study is taken in analogy with the studies of Witte (2015) (Fig. 2). The main legs are attached to the upper ring of the lander and supported by two secondary struts for each leg. The secondary struts are attached to the lower ring of the lander and are connected at approximately 55 cm above the footpad. Therefore, the lower part of the leg, called the primary strut, experience a bending moment when the footpad interacts with the soil. The leg has an outer diameter of 80 mm and a wall thickness of 5 mm. The outer diameter of the primary struts is 68 mm and its wall thickness is 9 mm while the secondary struts' outer diameter is 34 mm and the wall thickness is 4 mm. In this study the material properties of steel are assumed using a Young's modulus of 210 GPa and a Poisson's ratio of 0.2 for the legs and primary and secondary struts.

Fig. 1. Picture from Chandrayaan-3 on the lunar surface (ISRO, 2023).
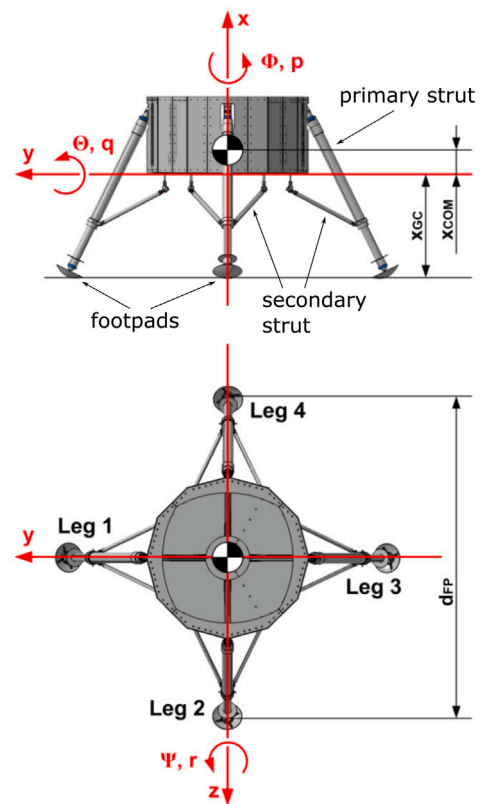

Fig. 2. LEM body-fixed coordinate system and principal dimensions definition (Witte, 2015).

The lander has a diameter of 120 cm and a height of 58 cm. It is modeled as a rigid body and therefore, cannot deform during the analysis. The geometrical properties are provided in Table 1. The numerical model of the lander is illustrated in Fig. 3.

The footpad geometry matches that of a spherical segment as shown in Fig. 4. The radius of the spherical segment is 36 cm and the projected
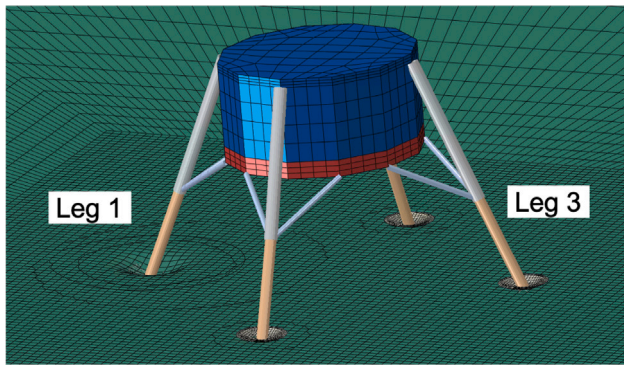
Fig. 3. Lander geometry and soil mesh at touch down on a slope with an inclination of 5° including the naming of the legs.

Table 1
Geometry and mass properties of the soft lander.

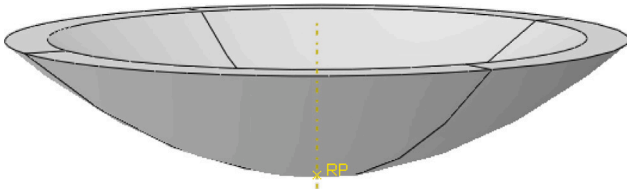| Property	Value Witte	Value study
mass m [kg]	310.7	311
center of mass x_{COM} [mm]	115	117
ground clearance x_{gc} [mm]	806	800
landing gear footprint d_{FP} [mm]	2400	2400

Fig. 4. Footpad geometry.

diameter of the footpad is 30 cm. The thickness of the footpad is taken to 1 cm although the footpad is modeled as a rigid body and therefore cannot deform. The footpads are fully connected in all translational directions to the primary struts while it can freely rotate around the connection point.

An aluminum honeycomb cartridge are included in the primary and secondary struts of real soft landers to prevent the lander from being damaged during touchdown. The cartridges absorb the impact energy due to plastic deformation once a predefined load limit is reached. In this numerical study the cartridges were not taken into account because the actual impact load on the legs is investigated and therefore should not be limited.

The best case in terms of leg loading occurs when all footpads touch the soil surface simultaneously. In turn the worst case occurs when one footpad touches the soil surface before the others, for example when the lander descends on a slope. In this study only the worst case is considered by rotating the lander such that always one single leg, Leg 1, is loaded first during touchdown. Fig. 3 shows the numerical model of a lander penetrating the surface of a slope with an inclination of 5°. Due to the inclination, Leg 1 touches the surface before the other legs are in contact. The largest distance between the footpad and soil surface occurs at Leg 3, which in turn touches the surface last.

Table 2
Soil properties for the three different soils used in this study.

soil	φ' [°]	c' [kPa]	E [kPa]	ν [−]	ρ [t/m³]
1	42	0, 5	180	0, 25	1, 5
2	30	0, 1	55	0, 33	1, 3
3	55	3, 5	500	0, 15	1, 9

3. Soil

3.1. Soil properties

Samples of lunar soil (regolith) were returned to Earth by the American Apollo missions and the Soviet space stations Luna-16, −20 and −24, see Slyuta (2014). Simulants have been developed because the quantity of these soil materials is limited. These simulants were designed to reproduce the mineralogy, grain-size distribution, and soil mechanical properties of lunar regolith (Weiblen and Gordon, 1988, Sture (2006)). Many studies have investigated these simulants. (e.g. Perkins and Madsen (1996); Klosky et al. (2000); Alshibli and Hasan (2009); Kobayashi et al. (2009); Arslan et al. (2010); Vrettos (2012); Venugopal et al. (2020)). The mechanical properties of lunar regolith were obtained by combining these results with those of the original soil material. Summarizing recent investigations and based on Carrier et al. (1991), Slyuta (2014) presented a range of mechanical properties that can be expected for the lunar regolith. In this study Soil 3 represents the upper range and Soil 2 the lower range of the mechanical properties presented in Slyuta (2014) to investigate the expected range of the footpad soil interaction. In addition the mechanical parameters for lunar regolith at the surface of intercrater areas obtained by Carrier et al. (1991) are used as Soil 1. The properties of lunar regolith change significantly with depth, see Carrier et al. (1991). Nevertheless, constant soil parameters are chosen in this study to demonstrate the influence of the soil parameters on the loading of the landing structure. The soil parameters for Soil 1 to 3 are listed in Table 2.

The variation in soil parameters shows uncertainty with respect to the soil properties in extraterrestrial applications. Looking at the moon, a very limited volume of real sample material exists, while for other objects, no material is available for soil testing at all. Additionally, this study deals with the landing of explorational space ships, meaning that there will be no soil investigation before landing.

The soil is modeled using a linear elastic, ideal plastic constitutive model with failure surface acc. to Mohr–Coulomb. The modeled soil body has a depth of 10 m and an additional height of 2 m above the soil surface. The volume above the soil surface is called the void area and consists of empty elements that do not contain any material, (see Section 4.1). The void area allows the soil to move into this area during the impact event of the footpads. The outer dimensions of the soil area is 50×50 m to ensure that the boundary conditions have no influence on the actual impact event.

3.2. Slope inclination

The initial soil stress state is applied as the initial condition for the numerical model. The soil stress state is defined as the vertical stress state depending on the depth z and the horizontal stress state is calculated by the vertical stress and earth pressure coefficient K_0. Gravity is taken as 1.62 m/s² to consider the lunar environment. To model an inclined slope, the initial stress state needs to be calculated using the numerical model in a separate calculation step. Alternatively, the initial stress state can be defined for every integration point within the model, see Dassault Systèmes (2022).

Because the calculation of the initial stress state by the numerical model itself involves an additional calculation step and accompanying deformations, a different approach is used. Instead of inclining the
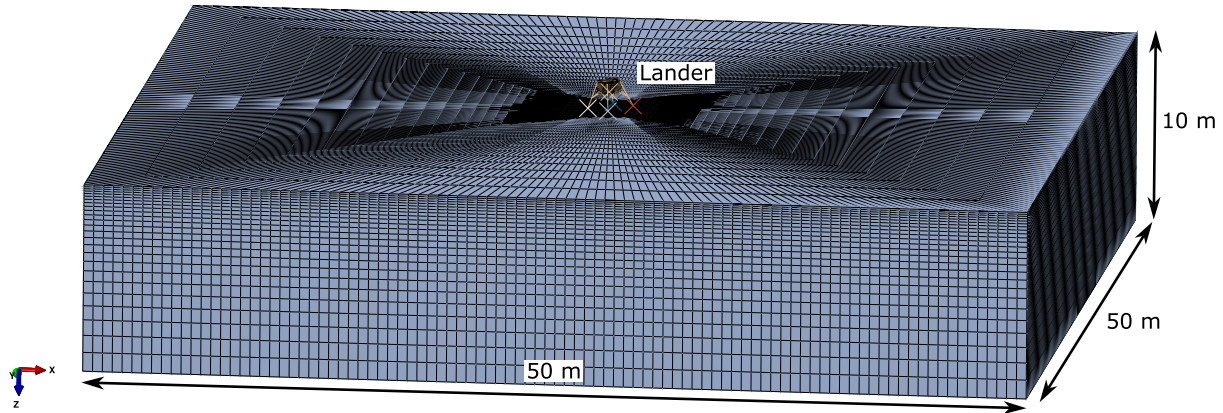
Fig. 5. Dimensions of the numerical model.

soil surface relative to the global coordinate system, the soft lander itself is rotated to ensure correct rotation between the soil surface and the lander. Hence, the direction of the lander's velocity as well as the direction of gravity must also be rotated. In doing so, the vertical direction of soil stress is perpendicular to the slope surface. To evaluate the calculations results, the rotation of the system needs to be considered to ensure a comparable coordinate system.

4. Numerical method

4.1. CEL-method

The Coupled Eulerian–Lagrangian-Method (CEL) can overcome mesh distortion problems in the simulation of large deformation processes. The CEL-method is briefly introduced in this section. Detailed information can be found in Dassault Systèmes (2022). It combines the advantages of the Lagrangian and Eulerian formulations. Both formulations differ in their description of the movement of small volumetric elements as a function of time.

The Lagrangian formulation describes the movement of a continuum as a function of material coordinates and time. Each node of the Lagrangian mesh moves along with the material during the simulation. Thus, the elements deform during the simulation and problems due to mesh distortion can occur. The surface of the continuum is specified precisely using this formulation. Furthermore, each Lagrangian element is dedicated to one type of material only. Lagrangian formulation is used in classical Finite-Element analyses and is often applied in solid mechanics.

In contrast Eulerian formulation describes the movement of a continuum as a function of spatial coordinates and time. The nodes of the Eulerian mesh are fixed during the simulation, such that the elements cannot deform. To realize the movement of a continuum, the material flows through the Eulerian mesh. Therefore, an Eulerian element is not dedicated to only one type of material. The element has to be filled with any material at all. With this formulation, no mesh distortion occurs and the simulation of large deformations is possible.

The Coupled Eulerian–Lagrangian-Method realizes an interaction between Lagrangian elements and Eulerian material using an Eulerian–Lagrangian contact formulation, see Dassault Systèmes (2022). The Eulerian time integration is realized by applying the "Lagrange-plus-remap" formulation. First, a traditional Lagrangian phase is calculated for each time increment and the nodes of the Eulerian mesh are temporarily fixed within the material. Therefore, the Eulerian elements can deform. Second, in the Eulerian phase, the so-called transport phase, the elements are tested for significant deformation. These elements are automatically remapped and the material flow through these elements

is calculated. The timestep has to be sufficiently small, so that no element distortions occur in one timestep.

The application of the CEL-Method to geomechanical problems involving large deformations was approved e.g. by Qiu et al. (2009, 2010), Bienen et al. (2011), Pucker and Grabe (2012) or Wang et al. (2015).

4.2. Discretization

The soil domain covers an area of 50×50 m and a depth of 10 m, see Fig. 5 The soil volume is discretized using C3D8R elements: a linear brick element with reduced integration and hour glass control, see Dassault Systèmes (2022). The element size is $0.1 \times 0.1 \times 0.1$ m at the soil surface in the near field of the lander. With increasing distance from the lander, the element size increases up to 1 m in height at the soil bottom and 4×0.5 m at the surface. The boundaries are fixed in normal direction at the sides and bottom of the soil domain. To reduce the influence of wave reflections at the boundaries, the distance between the lander and the boundaries is chosen to be 20 times the diameter of the lander's gear footprint. This approach has been successfully used e.g. in Henke (2012) and Grabe et al. (2013).

4.3. Contact

The Eulerian–Lagrangian contact formulation is an extension of the general contact formulation in Abaqus/Explicit (Dassault Systèmes, 2022). The contact algorithm automatically identifies the interface between the Lagrangian structure and Eulerian material. The Lagrangian structure pushes the material out of the Eulerian elements, and thus, the void areas evolve. Eulerian elements filled with material are not allowed in the region in which the Lagrangian structure is placed. Therefore, the Eulerian material is prevented from flowing into the elements underlying the Lagrangian structure. The Lagrangian structure can occupy Eulerian elements, such that the Eulerian mesh can be created independently from the contact interface.

Contact in the normal direction is defined as hard contact; therefore, no intersection is allowed. The tangential contact model is a Coulomb friction model with a friction coefficient of $\delta = 0.5$.

4.4. Damping

In Abaqus Explicit a bulk viscosity damping is associated with the volumetric straining, see Dassault Systèmes (2022). This approach improves the modeling of high-speed dynamics events, such as impact events. Based on extensive studies by Kelm (2004) on the influence of bulk viscosity on the soil response in dynamic compaction processes, a bulk viscosity of 0.42 and a quadratic bulk viscosity of 1.6 is chosen for this study.

Table 3
Parameter variations calculated in this study.

No.	v_v [m/s]	v_h [m/s]	soil no.	α [°]
1	2	0	1	0
2	2	0	1	5
3	2	0	1	15
4	2	0	2	0
5	2	0	2	5
6	2	0	2	15
7	2	0	3	0
8	2	0	3	5
9	2	0	3	15
10	1	0	1	5
11	1	0	2	5
12	1	0	3	5
13	3	0	1	5
14	3	0	2	5
15	3	0	3	5
16	2	0, 5	1	5
17	2	0, 5	2	5
18	2	0, 5	3	5
19	2	1, 0	1	5
20	2	1, 0	2	5
21	2	1, 0	3	5

4.5. Loading

The simulation is divided into three calculation steps. In the first step, the initial stresses of the soil and lunar gravity with $g = 1.62$ m/s^2 is applied. The lander is fixed at a distance of 1 cm between the bottom of the closest footpad and soil surface. Hence, any initial contact between the footpad and soil surface is avoided.

In the second step, the fixation of the lander is removed and velocities v_v in the vertical and v_h in the horizontal direction are applied to all elements of the lander. This allows the investigation of predefined touchdown velocities.

The velocity boundaries are removed in the third step, immediately before the footpad comes into contact with the soil. The lander still moves with the initiated velocities from step two whereas the velocities change owing to the influence of gravity and interaction with the soil.

5. Parametric study

In this study the influence of touchdown velocity in the vertical and horizontal directions, surface slope and soil properties was investigated. The range of touchdown velocities is taken in the vertical direction to $v_v = [1.0, 2.0, 3.0]$ m/s and in the horizontal direction to $v_h = [0.0, 0.5, 1.0]$ m/s, as described in Witte (2015). The influence of the surface slope is investigated by varying the surface slope angle with $\alpha = [0.0, 5.0, 15.0]°$ whereby the inclination of 15° corresponds to the maximum value considered for the Viking lander, see Muraca et al. (1975). Soil properties were varied by applying three sets of soil parameters (see Section 3). A total of 21 calculations were performed in this study, see Table 3.

6. Results

The calculated velocities of footpads 1 and 3 (attached to Leg 1 and Leg 3) are shown in Fig. 6. It can be seen, that the initial impact velocity of $v_z = 2.0$ m/s in vertical direction and $v_h = 0.0$ m/s in horizontal direction is applied correctly at $t = 0.0$ s. Footpad 1 touches the soil surface first if a slope inclination $\alpha > 0°$ is considered. For the case without slope inclination, as indicated by the green lines in Fig. 6, the vertical velocity decreases after the footpad is in contact with the soil surface. The vertical velocity reaches its minimum value of -1 m/s that is the corresponding maximum rebound velocity of the lander. The horizontal velocity of both footpads remain 0 m/s. Looking at the results obtained for the slop inclination, the blue and gray curves

in Fig. 6 show that the vertical velocity of footpad 3 increases before decreasing. This is because of the distance between footpad and soil is larger than the distance between footpad 1 and soil due to the surface inclination. Gravity still acts on the structure causing additional acceleration on the lander and footpad 3, and therefore increasing its vertical velocity until touchdown occurs. After contact with the soil surface, the vertical velocity of footpad 3 also starts decreasing. After approx 0.7 s, the vertical velocity of both footpads is approximately zero and the lander reaches a stable condition.

Once footpad 1 is in contact with the soil surface the friction resistance is mobilized and the lander starts to rotate if a slope inclination is considered. This rotation causes the leg to move horizontally in the upward direction of the slope (Fig. 6 bottom left). Due to gravity and the mobilized friction resistance, this uphill movement comes to a stop at approx. 0.1 s for the slope inclination of $\alpha = 5°$. Subsequently, the lander started to move in the downhill direction until the sliding resistance reached sufficient mobilization. Fig. 7 shows the corresponding shear stress at the contact area between the soil and footpad.

6.1. Influence of surface slope on the structural loads

The influence of the surface slope inclination on the time history of the touchdown forces of the primary struts in Leg 1 and 3 is shown in Figs. 8 and 9. Subsequently, the term leg is used to address the loading of the primary struts. The results are obtained from simulations using Soil 3 (Variation No. 7–9). Footpad 1 touches the soil surface first and the initial axial loading characteristic of Leg 1 is nearly independent of the slope inclination (Fig. 8 top). After the initial impact the lander starts to rotate, and footpad 3 touches the soil at a later point in time depending on the slope inclination (Fig. 8 bottom). It can be observed that the amplitude of axial loading of Leg 3 depends on the slope inclination.

The corresponding bending moments are shown in Fig. 9. The legs are inclined, and therefore point away from the main lander body (Fig. 3). Due to this geometrical boundary, the bending moments of the legs are significantly influenced by the slope inclination. In the case without surface inclination where all legs touch the soil surface at the same point in time, the legs are spread apart during touchdown and a bending moment is induced (see green curves for $\alpha = 0°$ in Fig. 9). Depending on the orientation of the local coordinate system of the leg, a positive bending moment occurs. If the surface is inclined, the same effect can be observed for Leg 1 at the beginning of touchdown (Fig. 9 top). Once footpad 1 penetrates the soil and the lander starts rotating, the footpad mobilizes the horizontal bearing capacity. Due to the rotation of the lander and the horizontal resistance of footpad 1, the bending moment of Leg 1 changes its sign and becomes negative, as shown by the blue lines at the top of Fig. 9. Ideally, this effect can lead to a reduction in the absolute maximum bending moment as in the case of an inclination of 5°.

The influence of the surface slope inclination on the maximum axial compression load of the primary struts in Leg 1 and Leg 3 is shown in Fig. 10. The axial compression load shows only a minor influence of the surface inclination (Fig. 10 top). Only for the high inclination of $\alpha = 15°$, the primary strut of Leg 3 experiences a higher axial compression load than the primary strut of Leg 1.

In addition, the maximum absolute bending moment of the primary struts in Leg 1 and Leg 3 shows a minor influence of the surface inclination (Fig. 10 bottom). Due to the effect of the change in sign of the moment and a corresponding reduction in the maximum absolute bending moment for the slope inclination of 5°, sometimes the primary strut in Leg 1 is higher loaded and sometimes the one in Leg 3. Nevertheless, the absolute maximum bending moments of both legs remain at a similar level.
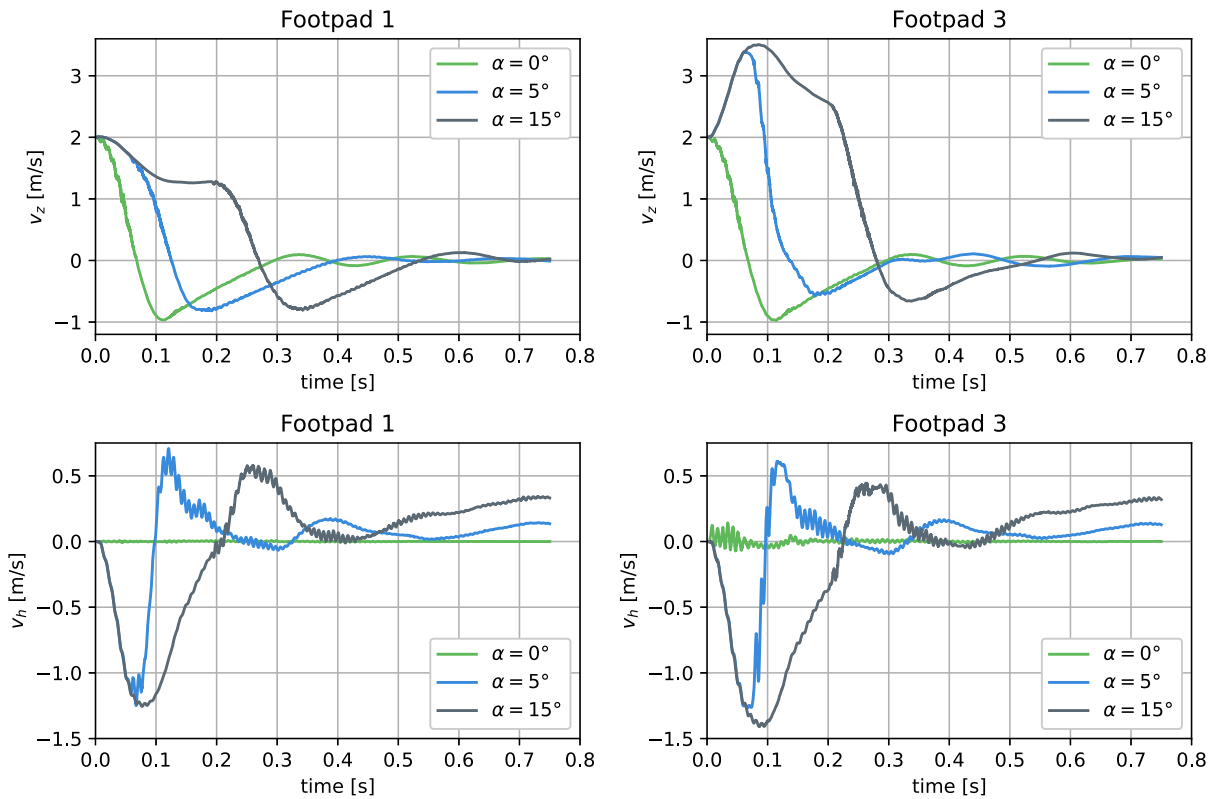
Fig. 6. Time history of the footpad velocities of Leg 1 (left) and Leg 3 (right) in vertical (top) and horizontal (bottom) direction for the touchdown process on a Soil 3 surface with different slope inclinations α, an impact speed of $v_z = 2.0$ m/s in vertical direction and $v_h = 0.0$ m/s in horizontal direction.
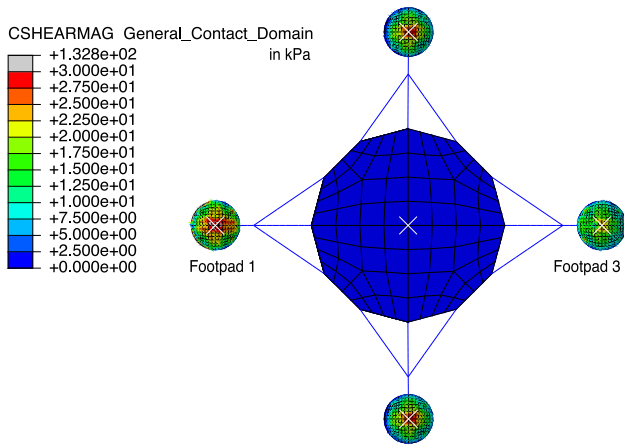

Fig. 7. Shear stresses at the footpad surfaces for s simulation time $t = 0.10$ s for Soil 3 with different slope of $\alpha = 5°$, an impact speed of $v_z = 2.0$ m/s in vertical direction and $v_h = 0.0$ m/s in horizontal direction.

6.2. Influence of vertical impact velocity on the structural loads

The variation in the vertical velocity shows a clear influence on the axial compression load of the primary struts in Leg 1 and Leg 3, see Fig. 11. All results are shown for a horizontal impact velocity of $v_h = 0$ m/s and a slope inclination of $\alpha = 0°$. As expected there is a clear increase in the axial compression load of the struts with increasing vertical impact velocity (Fig. 11 top). This effect is also shown in the increase in the maximum absolute bending moment with increasing vertical impact velocity (Fig. 11 bottom).
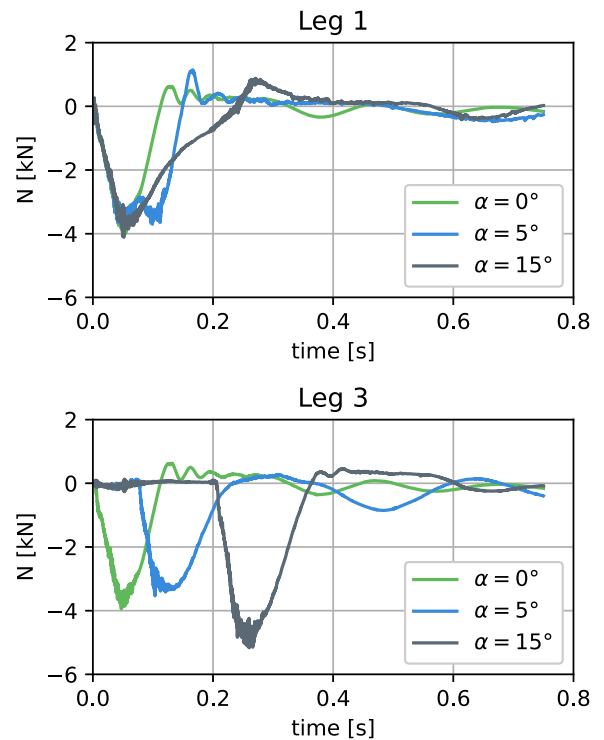

Fig. 8. Time history of axial loading of Leg 1 (top) and Leg 3 (bottom) depending on the surface slope inclination obtained for Soil 3.
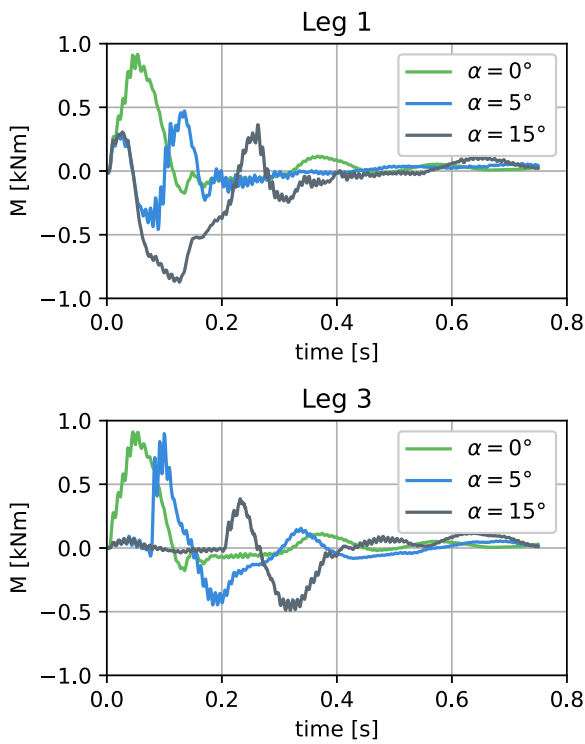
Fig. 9. Time history of bending moment of Leg 1 (top) and Leg 3 (bottom) depending on the surface slope inclination obtained for Soil 3.
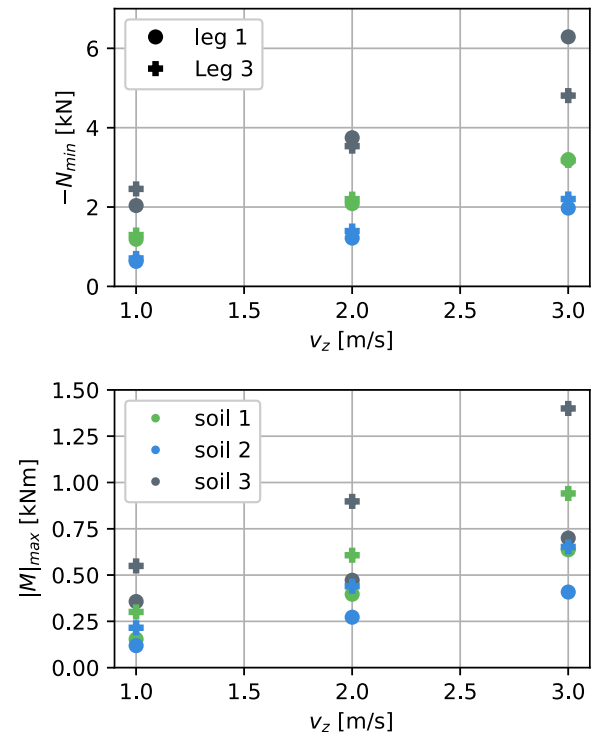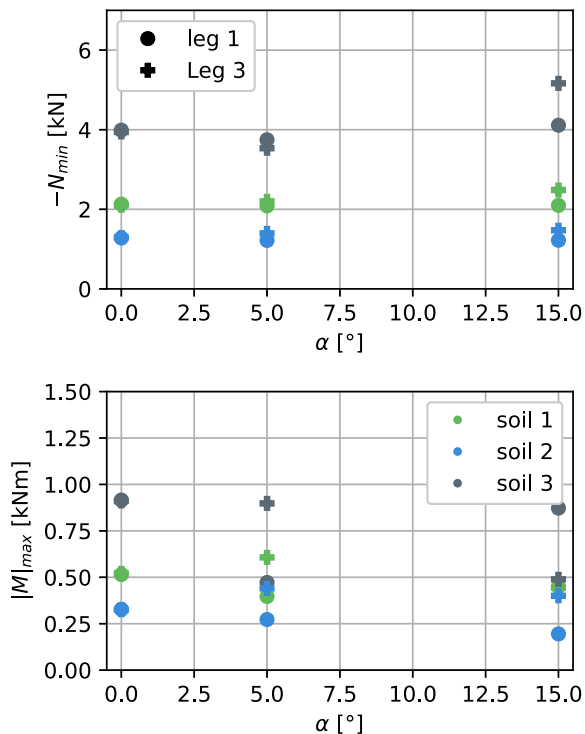
Fig. 11. Maximum axial compression load in (top) and maximum absolute bending moment of (bottom) the primary struts of Leg 1 and Leg 3 depending on the vertical impact velocity v_z for three different soils at horizontal impact velocity of 0 m/s and a surface inclination of $\alpha = 5°$.

is shown in Fig. 12. These results are obtained for a vertical impact velocity of $v_z = 2$ m/s and a slope inclination of $\alpha = 5°$. The horizontal impact velocity points downwards from the slope. Therefore, the axial compression force in the primary strut of Leg 1, which touches the surface first, decreases with increasing horizontal velocity (Fig. 12 top). However, the axial compression force in the primary strut of Leg 3 increases with increasing horizontal velocity. These effects do not counteract each other, and the maximum compression loads of both struts increase with the horizontal velocity. There are also some variations in the bending moment in the primary struts of the legs with increasing horizontal impact velocity (Fig. 12 bottom); however, this is not as significant as that observed for the axial compression loads.

6.4. Influence of soil properties

The influence of the soil properties on the maximum axial compression load and the maximum absolute bending moment of the primary struts of Leg 1 and Leg 3 are shown in Figs. 10–12. It can be clearly observed that the soil with the highest strength and stiffness parameters, Soil 3, results in the highest impact loads. In turn the soil with the lowest stiffness and strength parameters, Soil 2, results in the smallest impact loads.

7. Conclusion

Numerical simulations of soft lander touchdown are presented. The main influencing parameters slope inclination, impact velocities and soil properties were varied in this study. Overall, the influence of three different vertical and horizontal impact velocities, three slope inclinations and three soils was investigated, resulting in a total of 21 calculations, The results show a significant influence of the impact velocity and the soil properties while the slope inclination only has a minor impact. Nevertheless, the presented approach still implies important simplifications. The linear elastic, ideal plastic constitutive

Fig. 10. Maximum axial compression load in (top) and maximum absolute bending moment of (bottom) the primary struts of Leg 1 and Leg 3 depending on the surface inclination α for three different soils at vertical impact velocity of 2 m/s and horizontal impact velocity of 0 m/s.

6.3. Influence of horizontal impact velocity on the structural loads

The influence in the variation of the horizontal impact velocity on the axial compression load of the primary struts in Leg 1 and Leg 3
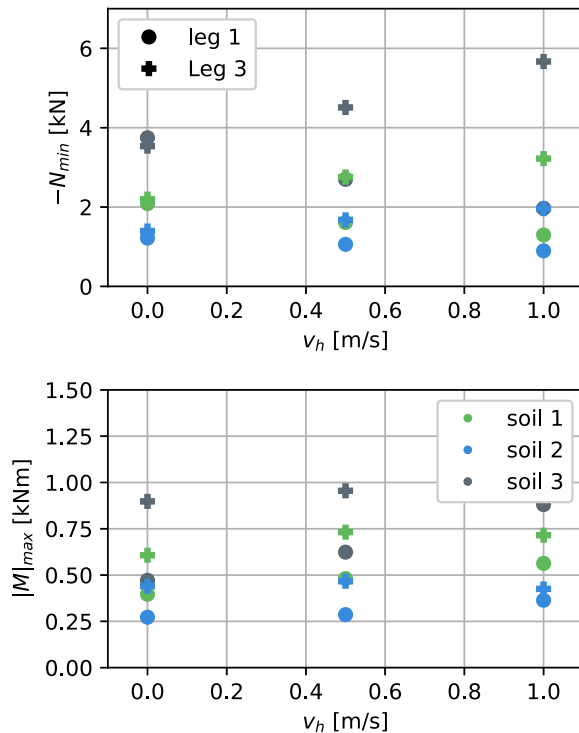
Fig. 12. Maximum axial compression load in (top) and maximum absolute bending moment of (bottom) the primary struts of Leg 1 and Leg 3 depending on the horizontal impact velocity v_h for three different soils at vertical impact velocity of 2 m/s and a surface inclination of $\alpha = 5°$.

model cannot accurately account for stress dependent stiffness or small strain effects. In addition, the potential effects of the lunar environment such as vacuum, electrostatic charge and temperature are neglected.

Ethical use disclaimer

In accordance with principles of responsible research and to prevent potential military applications, the author of this publication requests that the findings and information contained herein not be used for any military or defense-related purposes.

CRediT authorship contribution statement

T. Pucker: Conceptualization, Data curation, Formal analysis, Investigation, Methodology, Project administration, Resources, Validation, Visualization, Writing – original draft.

Declaration of competing interest

The authors declare that they have no known competing financial interests or personal relationships that could have appeared to influence the work reported in this paper.

Data availability

Data will be made available on request.

References

Alshibli, K.A., Hasan, A., 2009. Strength properties of JSC-1A lunar regoltih simulant. J. Geotech. Geoenviron. Eng. 135 (5), 673–679.

Arslan, H., Baliste, S., Sture, S., 2010. Engineering properties of lunar soil simulant JSC-1A. J. Aerosp. Eng. 23 (1), 70–83.

Bienen, B., Henke, S., Pucker, T., 2011. Numerical study of the bearing behaviour of circular footings penetration into sand. In: Proc. of 13th International Conference of International Association for Computer Methods and Advances in Geomechanics. IACMAG, pp. 939–944.

Carrier, W.D.I., Olhoeft, G.R., Mendell, W., 1991. Physical properties of the lunar surface. In: Lunar Sourcebook. pp. 475–594.

Che, A., Zhu, R., Jiang, M., 2018. Dynamica response of lunar soil caused by landing impact. KSCE J. Civ. Eng. 22 (11), 4282–4292.

Dassault Systèmes, 2022. Abaqus user manual version 2022.

Grabe, J., Henke, S., Pucker, T., Hamann, T., 2013. CEL simulations for soil plugging, screwed pile installation and deep vibration compaction. In: International Conference on Installation Effects in Geotechnical Engineering 2013 in Rotterdam/Netherlands. pp. 118–127.

Henke, S., 2012. Large deformation numerical simulations regarding soil plugging behaviour inside open-ended piles. In: Proceedings of 31st International Conference on Ocean, Offshore and Artic Engineering (OMAE) 2012 in Rio de Janeiro/Brazil. Electronically Published under OMAE2012-830389.

ISRO, 2023. Chandrayaan-3. URL https://www.isro.gov.in/chandrayaan3_gallery.html.

Ji, S., Liang, S., 2021. DEM-FEM-MBD coupling analysis of landing process of lunar lander considering landing mode and buggering mechanism. Adv. Space Res. 68, 1627–1643.

Kelm, M., 2004. Numerische Simulation der Verdichtung rolliger B"oden Mittels Vibrationswalzen (Ph.D. thesis). Technische Universit"at Hamburg-Harburg, Institut f"ur Geotechnik und Baubetrieb, Heft 6.

Klosky, J.L., Sture, S., Ko, H.-Y., Barnes, F., 2000. Geotechnical behavior of JSC-1 A lunar soil simulant. J. Aerosp. Eng. 13 (4), 133–138.

Kobayashi, T., Ochiai, H., Suyama, Y., Aoki, S., Yasufuku, N., Omine, K., 2009. Bearing capacity of shallow foundations in a low gravity environment. Soils Found. 49 (1), 115–134.

Liang, D., Wang, G., Zhang, P., 2022. Landing dynamic analysis for leg of lunar lander using nonlinear finite element method. Adv. Astronaut. Sci. Technol. 5, 235–240.

Muraca, R., Campbell, J.W., King, C.A., 1975. A Monte Carlo analysis of the viking lander dynamics at touchdown.

NASA, 1968. Bendix Corporation, Lunar Module Soil Mechanics Study, vol. I, NASA, Houston, Texas, May 1968.

Perkins, S.W., Madsen, C.R., 1996. Mechanical and load- settlement characteristics of two lunar soil simulants. J. Aerosp. Eng. 9, 1–9.

Pucker, T., Grabe, J., 2012. Numerical simulation of the installation process of full displacement piles. Comput. Geotech. 45, 93–106. http://dx.doi.org/10.1016/j.compgeo.2012.05.006.

Qiu, G., Henke, S., Grabe, J., 2009. Applications of coupled Eulerian Lagrangian method to geotechnical problems with large deformations. In: Proc of SIMULIA Customer Conference 2009 in London, 420–435.

Qiu, G., Henke, S., Grabe, J., 2010. Application of a coupled Eulerian-Lagrangian approch on geomechanical problems involving large deformation. Comput. Geotech. http://dx.doi.org/10.1016/j.compgeo.2010.09.002.

Slyuta, E.N., 2014. Physical and mechanical properties of the lunar soil (A Review). Solar Syst. Res. 58 (5), 330–353.

Sture, S., 2006. A review of geotechnical properties of lunar regolith simulants. In: Malla, R.B., Bininda, W.K., Maji, A.K. (Eds.), Earth & Space 2006: Engineering, Construction, and Operations in Challenging Environment. http://dx.doi.org/10.1061/40830(188)90.

Venugopal, I., Prabu, T., Muthukkumaran, K., Annadurai, M., 2020. Development of a novel lunar highland soil simulant (LSS-ISAC-1) and its geotechnical properties for Chandrayaan missions. Planet. Space Sci. 194 (105116).

Vrettos, C., 2012. Shear strength investigations for a class of extraterrestrial analogue soils. J. Geotech. Geoenviron. Eng. 138 (4), 508–515.

Wang, D., Bienen, B., Nazem, M., Tian, Y., Zheng, J., Pucker, T., Randolph, M.F., 2015. Large deformation analyses in geotechnical engineering. Comput. Geotech. 65, 104–114.

Wang, Z., Chen, C., Chen, J., Zheng, G., 2023. 3D soft-landing dynamica theoretical model of legged lander: Modelling and analysis. Aerospace 10, 811. http://dx.doi.org/10.3390/aerospace10090811.

Weiblen, P.W., Gordon, K., 1988. Characteristics of a simulant for lunar surface materials. In: Proc. 2nd Conf. Lunar Bases Space Activities 21st Century, Lunar and Planetary Institute, Houston, TX.

Witte, L., 2015. Touchdown Dynamics and the Probability of Terrain Related Failure of Planetary Landing Systems ? A Contribution to the Landing Safety Assessment Process (Ph.D. thesis). Universität Bremen.

Witte, L., Schröder, S.E., R., B., 2010. Touchdown - down dynamics and terrain interaction of planetary landing systems. In: Global Lunar Conference.

Yin, C., Schiavone, P., Quan, Q., Tang, D., Deng, Z., 2023. Normal force on the asteroid regoltih generated by the impact of lander footpad. Acta Astronaut. 202, 229–251. http://dx.doi.org/10.1016/j.actaastro.2022.10.032.

Yuncheng, L., Liben, K., Zhenjua, Z., Rongrong, Z., Cong, J., Meng, Z., 2020. Simulation analysis of dynamic behavior of lander footpad impact on lunar regolith. J. Deep Space Explor. 7 (2), 171. http://dx.doi.org/10.15982/j.issn.2095-7777.2020.20190313002.

Zheng, G., Nie, H., Chen, J., Chen, C., Lee, H.P., 2018. Dynamic analysis of lundar lander during soft landing using explicit finite element method. Acta Astronaut. 148, 69–81. http://dx.doi.org/10.1016/j.actaastro.2018.04.014.